optica

Tomographic diffractive microscopy with isotropic resolution

Bertrand Simon,[1] Matthieu Debailleul,[1] Mounir Houkal,[2] Carole Ecoffet,[2] Jonathan Bailleul,[1] Joël Lambert,[1] Arnaud Spangenberg,[2] Hui Liu,[3] Olivier Soppera,[2] and Olivier Haeberlé[1,*]

[1]Laboratoire Modélisation Intelligence Processus et Systèmes MIPS–EA2332, Université de Haute-Alsace (UHA), 61 rue Albert Camus, F-68093 Mulhouse Cedex, France
[2]Institut de Science des Matériaux de Mulhouse IS2M, Université de Haute-Alsace (UHA), CNRS UMR 7361,15 rue Jean Starcky, BP 2488, F-68057 Mulhouse Cedex, France
[3]Institut de Génétique et de Biologie Moléculaire et Cellulaire IGBMC, Université de Strasbourg (UniStra), CNRS UMR 7104, INSERM U964, 1 rue Laurent Fries, F-67404 Illkirch Cedex, France
*Corresponding author: olivier.haeberle@uha.fr

Received 20 December 2016; revised 17 March 2017; accepted 21 March 2017 (Doc. ID 283212); published 19 April 2017

Microscopy techniques allowing observation of unlabeled samples have recently experienced a regain of interest. In particular, approaches based on recording of the optical field diffracted by the specimen, in amplitude and phase, have proven their capacities for biological investigations. When combined with variations of specimen illumination, tomographic acquisitions are possible. One limitation of previously developed approaches is the anisotropic resolution, characteristic of all transmission microscopes. In this context, an instrument, characterized by isotropic high-resolution 3D imaging capabilities, is still awaited. For the first time, to the best of our knowledge, we have developed tomographic diffractive microscopy combining specimen rotation and illumination rotation, which delivers images with (almost) isotropic resolution below 200 nm. The method is illustrated by observations of nanoscopic fiber tips, microcrystals and pollens, and should be helpful for characterizing freestanding natural (diatoms, spores, red or white blood cells, etc.) or artificial samples.

OCIS codes: (180.0180) Microscopy; (180.6900) Three-dimensional microscopy; (180.3170) Interference microscopy; (090.0090) Holography; (090.1995) Digital holography; (090.2880) Holographic interferometry.

https://doi.org/10.1364/OPTICA.4.000460

Fluorescence microscopy is the tool of choice for functional investigations, thanks to the immense variety of labels, and to the development of fluorescence nanoscopy, recognized by the attribution of the Nobel Prize in Chemistry 2014 for the development of super-resolved fluorescence microscopy. But for scientists who do not want to, or cannot, use fluorescence or electron microscopy, imaging capabilities of conventional optical microscopes are still limited.

Among the various techniques developed to image non-fluorescent samples, phase microscopy has already found many applications, in biology as well as material science [1–5].

Tomographic diffractive microscopy [6–14] (TDM, also referred to as synthetic aperture microscopy, tomographic phase microscopy, phase nanoscopy, optical diffraction tomography, etc.; see Ref. [14] for a general introduction to these techniques) is an extension of phase microscopy, combining amplitude and phase imaging with a variation of the conditions of illumination and/or the conditions of observation. It relies on computer-assisted image reconstruction of the sample, from the electromagnetic field it diffracts. The simplest approach considers that the first Born approximation is valid, so that the diffracted field is linked to the 3D Fourier transform of the specimen index of refraction distribution [15].

Figure 1 describes the acquisition process for common holographic and tomographic configurations, highlighting the interest of this technique, in terms of sample frequency acquisition. In the Fourier domain of spatial frequencies, the diffracted field is represented by the k_{diff} wavevectors depicting the Ewald sphere. In holographic microscopy, one direction of illumination, usually parallel to the optical axis (depicted by k_{ill} vector), is used, and because of the limited numerical aperture (NA) of the microscope objective, only a cap of sphere of k_{diff} vectors is detected [Fig. 1(a)]. The elastic scattering condition links the registered field to specimen frequencies by momentum conservation $k_{\mathrm{obj}} = k_{\mathrm{diff}} - k_{\mathrm{ill}}$. The lateral extension of the k_{obj} cap of sphere provides a good lateral resolution, whereas its axial extension being very restricted, the imaging capabilities along the optical axis are strongly affected [8–12].

To improve the resolution, one can use inclined illumination [6–12], shifting the detected k_{diff} vectors towards higher k_{obj} vectors [Fig. 1(b)]. When many illuminations are sequentially used, a virtual condenser is synthetized, and the optical transfer function (OTF) support is extended, and filled [6] [Fig. 1(c)]. The lateral and axial resolutions are improved and true 3D imaging becomes possible [8–12]. However, the smaller extension of the OTF

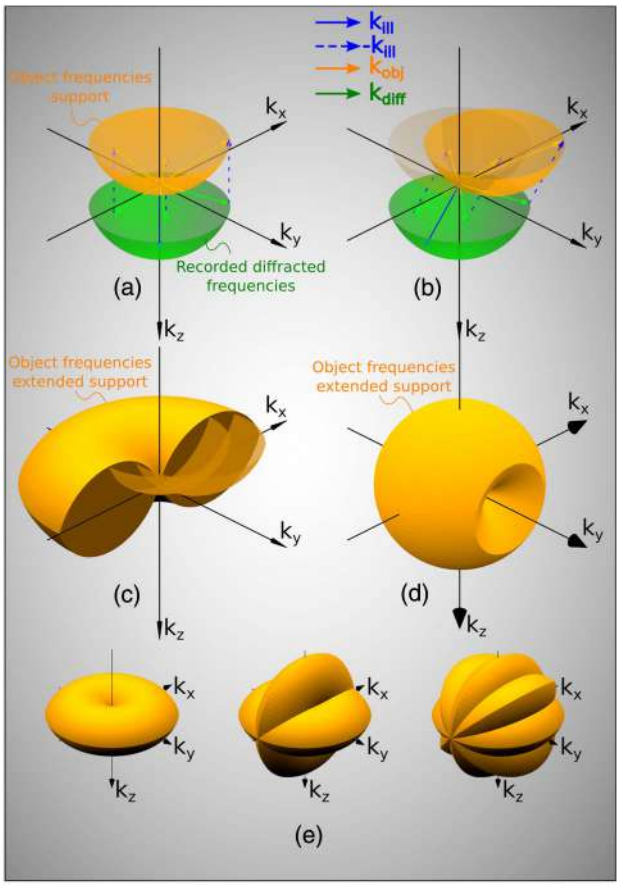

Fig. 1. Construction of the OTF for various configurations of TDM. (a) Digital holographic microscopy. The recorded k-vectors k_{diff} are shifted back according to momentum conservation to provide object vectors k_{obj}: the OTF depicts a cap of sphere of a large lateral, but limited, longitudinal extension. (b) When using inclined illumination in TDM-IR, the same positions of the k_{diff} vectors provide new k_{obj} vectors. (c) A large set of illuminations results in a filled and extended OTF: TDM-IR provides improved-resolution, higher quality 3D images. Note, however, the presence of a so-called "missing cone" along the optical axis z, limiting longitudinal resolution and sectional capabilities. (d) OTF for TDM-SR. An almost completely filled sphere is obtained, but of lesser extension than in the previous case. (e) OTFs obtained for TDM-IRSR when combining TDM-IR with 0°, (0°; 90°) and (0°; 45°; 90°; 135°) specimen rotations [displayed at half-scale compared with (a)–(d)]. A missing-cone-free and extended support is obtained, showing that TDM-IRSR can deliver 3D, isotropic- and improved-resolution images. See also Visualization 1.

along k_z direction (optical axis) and the so-called "missing cone" translates into lower axial resolution, and limits sectioning capabilities [12], as for any transmission microscope.

Another approach consists of rotating the sample [Fig. 1(d)]: an almost complete spherical OTF is obtained, albeit with a smaller extension, and a small set of missing frequencies does exist along the rotation axis [16] (here y axis), slightly degrading the resolution in this direction [17]. This configuration also requires a large number of sample rotations to properly fill the OTF [17–19].

In order to simultaneously obtain improved- and isotropic-resolution images, one can combine [13] illumination and specimen rotations. Figure 1(e) shows the OTF support for 1, 2, and 4 views: few rotations permit obtaining a quasi-spherical, extended OTF (see also Visualization 1 for an animated construction of the frequency supports). Theoretically proposed in Ref. [13] and studied by simulations, such a configuration had, however, not been tested experimentally up to now. The lateral and axial extensions of the frequency support for holographic microscopy are given, respectively, by [6]

$$\Delta\nu_{x,y}^{\text{Holo}} = \frac{2n\,\sin\,\theta}{\lambda} \quad \text{and} \quad \Delta\nu_{z}^{\text{Holo}} = \frac{n(1-\cos\,\theta)}{\lambda}.$$

For TDM with illumination rotation (TDM-IR), one doubles the lateral frequency support [6] and

$$\Delta\nu_{x,y}^{\text{TDM-IR}} = \frac{4n\,\sin\,\theta}{\lambda} \quad \text{and} \quad \Delta\nu_{z}^{\text{TDM-IR}} = \frac{2n(1-\cos\,\theta)}{\lambda}.$$

For TDM with sample rotation (TDM-SR), one gets [13]

$$\Delta\nu_{x,z}^{\text{TDM-SR}} = \frac{4n\,\sin(\theta/2)}{\lambda} \quad \text{and} \quad \Delta\nu_{y}^{\text{TDM-SR}} = \frac{2n\,\sin\,\theta}{\lambda}.$$

When combining both approaches (TDM-IRSR), one obtains

$$\Delta\nu_{x,y,z}^{\text{TDM-IRSR}} = \frac{4n\,\sin\,\theta}{\lambda}.$$

To overcome the resolution limitations of previously developed TDM systems [6–12,17–19], we have developed TDM-IRSR by adapting a special sample rotation system, compatible with a high-NA objective and a condenser ($NA_{obj} = NA_{con} = 1.4$), onto our previously built TDM-IR system. The system is based on a modified Mach–Zehnder interferometer, the angle of incidence of the illumination beam (633 nm or 475 nm) being controlled using a fast tip–tilt mirror. The diffracted and reference beams are recombined prior to detection, in an off-axis configuration. Interferograms are corrected for residual aberrations [20] and merged in Fourier space. Image reconstruction can be performed under a Born or Rytov approximation (see also Supplement 1 for more details about the experimental setup).

To illustrate the superior imaging capabilities of this new instrument, a tapered optical fiber is first imaged at 475 nm illumination. The heat-and-pull technique [21] produces very sharp tips, a few micrometers long, and with a tip end diameter below 100 nm. These characteristics make of such an object a good test pattern to compare the quality of the images obtained from different configurations.

Figures 2(a)–2(c) show (x–y), (x–z), and (y–z) views, respectively, of the 3D image of the fiber tip, obtained in TDM-IR. The high lateral resolution permits observing the 1 μm long fiber tip in the (x–y) view. In Fig. 2(a), a 95 nm resolution (or $\lambda/3.5$NA, as in Ref. [8]) is estimated (with classical lateral resolution in incoherent imaging, $R_{lat} = \lambda/2\text{NA} = 170$ nm). Note that measuring resolution in coherent imaging may be challenging [22] (see Supplement 1 for details about resolution estimation). The system suffering from the previously mentioned z-axis elongation, the sharp tip is, however, not visible in the (x–z) view [Fig. 2(b)]. Furthermore, the fiber itself is not observed as a cylindrical object [Fig. 2(c)].

In order to perform TDM-IRSR, the fiber is connected to a stepper motor, to ensure rotation [23]. Figures 2(d)–2(f) show the fiber, after combining four views obtained at 0°, 54°, 90°, and 126°. The section of the fiber now almost depicts a disc and the sharp tip is visible in both (x–y) and (z–y) views (see Supplement 1 for details about the data fusion procedure). A lateral resolution of 150 nm and a longitudinal resolution of 180 nm are obtained (with classical longitudinal resolution, $R_{long} = n\lambda/(\text{NA})^2 = 490$ nm). These

indicate that the fusion process is not perfect, the lateral resolution being slightly degraded, but a large gain in longitudinal resolution is indeed obtained. Higher lateral resolutions have been reported [10,12], but such a high and (almost) isotropic resolution in transmission microscopy is a novelty, which constitutes a breakthrough in the domain and should permit more precise investigations, for example, at the cellular level in biology.

To observe specimens, like pollens, diatoms or microcrystals, we attach them to an optical fiber by photopolymerization (Supplement 1 describes in detail the sample attachment procedure), the fiber being used as both a sample holder and a rotator.

Figures 3(a)–3(c) depict a *Bellis perennis* pollen grain, imaged at 633 nm. Figure 3(a) shows an (x–y) view, highlighting the characteristic spikes of these pollens. Note the photopolymer tip, which connects the pollen grain to ensure controlled rotation. Figure 3(b) shows an (x–z) view, the spikes not being visible along that direction. Figure 3(c) shows the superimposition of three views of the pollen grain, after 0° (red), 54° (green) and 108° (blue) rotations. The spikes visible in one view are not identifiable in the others, but data fusion should permit delivering images with isotropic characteristics.

Figures 3(d)–3(h) illustrate image quality gain for a zeolite crystal imaged with one view, Fig. 3(d), and after fusion of eight views. Note the microbubbles attached to the crystal, which appear spherical in Figs. 3(e) and 3(f), but noticeably elongated in Fig. 3(d) (see also Visualization 2): when imaging cells, precise shape and volume determination of smaller organelles could be hampered by this anisotropy when observed with TDM-IR (TDM-SR delivering anyway lower-resolution images), whereas TDM-IRSR would allow much more precise measurements.

Figure 4 shows a *Betula pendula* triporate pollen grain. TDM delivers dual views of the sample, identifying refraction and absorption in two separate images [14]. The contact sheet depicts volumetric cuts in the z direction (x–y views) through the index image, Fig. 4(a), and the absorption image, Fig. 4(b), highlighting the inner structures of the pollen grain, its double-layer outer structure (arrow) with chambers separating the inner and outer walls (vestibulum), and protruding pores (double-headed arrow) (see also Visualization 3). The refraction index (RI) is calibrated from the known RIs of the immersion medium and of the photopolymer tip. The pollen walls are composed of highly refractive components like sporopollenins and cellulose [24], while the vestibulum is of lower RI. Some regions of the nucleus exhibit high RI [25], and the absorptive components seem confined to the interior of the pollen.

Such clear discrimination between the refractive and absorptive parts of a sample, in 3D and at high resolution, also constitutes a novelty. Refraction images have proven to constitute a useful tool for biological investigations [7,9–11,26], whereas absorption images have not been used up to now, but indeed give complementary information [8,12,27–29].

Figures 4(c) and 4(d) show 3D views of the absorption within the pollen and the complex index of refraction (refraction and absorption), respectively. Note the photopolymer tip, identifiable in Fig. 4(d), but not in Fig. 4(c). The absorption image (yellow) is indeed embedded within the refraction image (cyan), as shown in Fig. 4(e), which is a cut through the pollen: attenuation is confined to the inner wall or intine, whereas the outer wall, or exine, is refractive only (see also Visualization 4). Finer characterization of pollen grain's optical properties would, for example, be necessary in view of better understanding their contribution by direct absorption and scattering to local radiative forcing. Current models, even if geometrically very elaborate, usually neglect absorption [30]. The method we propose may contribute to address this limitation.

In conclusion, we have developed a tomographic diffractive microscope combining illumination and specimen rotations, which circumvents an important limitation in transmission microscopy:

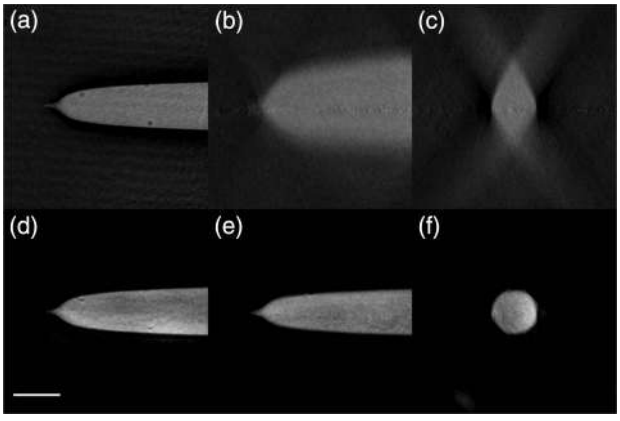

Fig. 2. Lateral, axial and sagittal views of a tapered fiber tip, obtained by heat-and-pull technique and observed with TDM. (a) With TDM-IR. (x–y) lateral plane view: note the excellent lateral resolution. (b) (x–z) axial plane view: the missing cone in this configuration induces low resolution along the optical axis and the fiber tip is not visible. (c) (y–z) sagittal view: the low sectional capabilities of TDM-IR translate into a deformed image of the specimen—the fiber section is not circular. Panels (d)–(f) show the same fiber observed with TDM-IRSR. The fiber tip is now clearly visible in both (x–y) and (x–z) views and the fiber section is almost circular, as expected. Combination of four acquisitions after specimen rotations of 0°, 54°, 90°, and 126° steps. Scale bar: 3 μm.

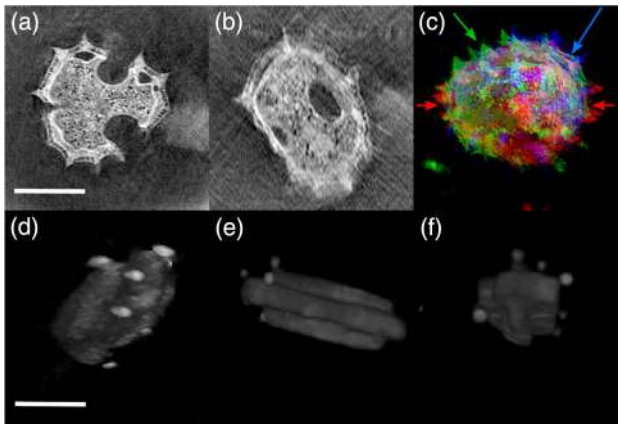

Fig. 3. *B. perennis* pollen grain and zeolite crystal observed with TDM. (a) (x–y) view for one angle of acquisition (TDM-IR). The polymer fiber tip, used to rotate the sample, is visible. Note the characteristic spikes of this type of pollen. (b) (x–z) view in TDM-IR. Note the elongation along the optical axis, and the vanishing aspect of the pollen surface, due to the missing cone. The spikes are hardly recognizable. (c) Colored superimposition of three views of the same pollen grain for three angles of rotation of the sample (red, 0°; green, 54°; and blue, 108°). Note the complementarity of the data (colored arrows): fusion should permit delivering isotropic-resolution images. Scale bar: 10 μm. Panels (d)–(f) show images of a zeolite crystal for (d) one angle of acquisition (TDM-IR) and [(e, f)] after eight acquisitions and data fusion (TDM-IRSR). The crystal is better imaged; the surrounding small bubbles attached to the crystal are spherical with TDM-IRSR, whereas they appear elongated with TDM-IR only. Scale bar: 10 μm. See also Visualization 2.

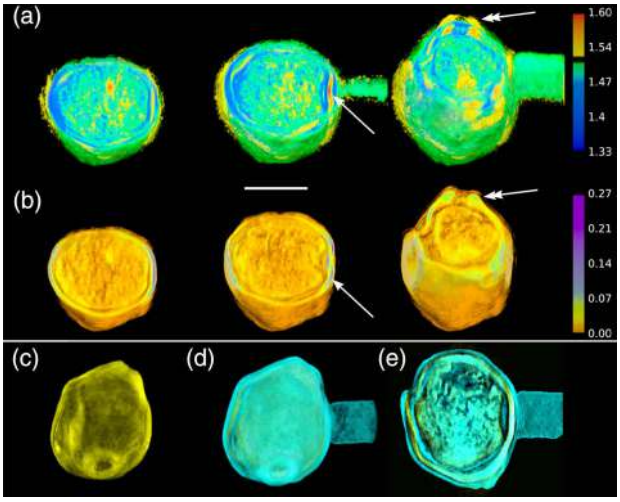

Fig. 4. *Betula* pollen grain observed with TDM. Panels (a) and (b) show volumetric cuts (x–y views) through the 3D index of refraction image and absorption image, respectively. Note the higher index of refraction of the pollen walls, especially near the pores (double-headed arrow), and the double-layer outer wall (arrow). Scale bar: 10 μm. See also Visualization 3. (c) Outer view of the pollen: image of the absorption component, displayed in yellow. (d) Outer view of the pollen: image of the complex index of refraction, with the refractive component displayed in cyan. The photopolymer tip used to handle the sample is purely refractive, and, hence, visible on the index component but not on the absorption image. (e) (x–y) cut through the pollen. Note that the absorptive components are confined to the interior of the pollen, nucleus and intine, and absent from the exine. See also Visualization 4.

it delivers images with an isotropic and improved resolution, and also with clear distinction of refraction and attenuation, two quantities that are usually mixed in intensity-only microscopy [14]. Possible extensions of this technique include isotropic-resolution, combined TDM-fluorescence microscopy [12,28], and spectral TDM imaging [31], as attenuation is often strongly wavelength-dependent.

Biological research [1–5] on freestanding specimens (for example, microplankton science, palynology, bacteriology, hematology, gamete and fertilization studies) as well as research on transparent materials [5] like photopolymers, structured optical fibers, textile fiber science, micro- and nanofabrication characterization, microcrystal could benefit from the superior imaging capabilities of such an instrument.

Using glass microcapillaries [17–19,25], or contact-free sample rotation systems, based on optical [32,33] or dielectrophoretic forces [34,35] may also facilitate the use of this technique with living, freestanding samples, like red or white blood cells, egg cells, pollens or unicellular organisms (diatoms, radiolarians). For living specimens, however, the oil-immersion objectives used throughout this work should be replaced with water-immersion objectives (with slightly lowered resolution).

Alternatively, if observing larger inert samples, low-NA, long-working-distance air objectives could be used. For samples presenting high indices of refraction, the technique we have developed could also benefit from advanced numerical reconstruction methods, which allow true super-resolution in far-field microscopy [36].

Funding. Agence Nationale de la Recherche (ANR) (ANR-10-PDOC-0009 Nanoquenching, ANR-11-JS10-0003 OSIRIS).

See Supplement 1 for supporting content.

REFERENCES

1. K. Myung, *Digital Holographic Microscopy: Principles, Techniques, and Applications*, Springer Series in Optical Science (Springer, 2011), Vol. **162**.
2. G. Popescu, *Quantitative Phase Imaging of Cells and Tissues* (McGraw-Hill, 2011).
3. K. Lee, K. Kim, J. Jung, J. Heo, S. Cho, S. Lee, G. Chang, Y. Jo, H. Park, and Y. Park, Sensors **13**, 4170 (2013).
4. B. Kemper, "Digital holographic microscopy: quantitative phase imaging and applications in live cell analysis," in *Handbook of Coherent-Domain Optical Methods*, V. V. Tuchin, ed. (Springer, 2013).
5. B. Bhaduri, C. Edwards, H. Pham, R. Zhou, T. Nguyen, L. Goddard, and G. Popescu, Adv. Opt. Photon. **6**, 57 (2014).
6. V. Lauer, J. Microsc. **205**, 165 (2002).
7. W. Choi, C. Fang-Yen, K. Badizadegan, S. Oh, N. Lue, R. R. Dasari, and M. S. Feld, Nat. Methods **4**, 717 (2007).
8. M. Debailleul, B. Simon, V. Georges, O. Haeberlé, and V. Lauer, Meas. Sci. Technol. **19**, 074009 (2008).
9. Y. Park, M. Diez-Silva, G. Popescu, G. Lykotrafitis, W. Choi, M. S. Feld, and S. Suresh, Proc. Natl. Acad. Sci. USA **105**, 13730 (2008).
10. Y. Cotte, F. Toy, P. Jourdain, N. Pavillon, D. Boss, P. Magistretti, P. Marquet, and C. Depeursinge, Nat. Photonics **7**, 113 (2013).
11. T. Kim, R. Zhou, M. Mir, S. Derin Babacan, P. Scott Carney, L. L. Goddard, and G. Popescu, Nat. Photonics **8**, 256 (2014).
12. M. Debailleul, V. Georges, B. Simon, R. Morin, and O. Haeberlé, Opt. Lett. **34**, 79 (2009).
13. S. Vertu, J. Flügge, J.-J. Delaunay, and O. Haeberlé, Central Eur. J. Phys. **9**, 969 (2011).
14. O. Haeberlé, K. Belkebir, H. Giovannini, and A. Sentenac, J. Mod. Opt. **57**, 686 (2010).
15. E. Wolf, Opt. Commun. **1**, 153 (1969).
16. S. Vertu, J.-J. Delaunay, I. Yamada, and O. Haeberlé, Central Eur. J. Phys. **7**, 22 (2009).
17. Y.-C. Lin and C.-J. Cheng, J. Opt. **16**, 065401 (2014).
18. M. Kujawińska, W. Krauze, A. Kus, J. Kostencka, T. Kozacki, B. Kemper, and M. Dudek, Int. J. Optomechatron. **8**, 357 (2014).
19. A. Kus, M. Dudek, B. Kemper, M. Kujawińska, and A. Vollmer, J. Biomed. Opt **19**, 46009 (2014).
20. H. Liu, J. Bailleul, B. Simon, M. Debailleul, B. Colicchio, and O. Haeberlé, Appl. Opt. **53**, 748 (2014).
21. M. Xiao, J. Nieto, J. Siqueiros, and R. Machorro, Rev. Sci. Instrum. **68**, 2787 (1997).
22. R. Horstmeyer, R. Heintzmann, G. Popescu, L. Waller, and C. Yang, Nat. Photonics **10**, 68 (2016).
23. A. Barty, K. A. Nugent, A. Roberts, and D. Paganin, Opt. Commun. **175**, 329 (2000).
24. S. Barrier, "Physical and chemical properties of sporopollenin exine particles," Ph.D. dissertation (University of Hull, 2008).
25. F. Charrière, A. Marian, F. Montfort, J. Kuehn, T. Colomb, E. Cuche, P. Marquet, and C. Depeursinge, Opt. Lett. **31**, 178 (2006).
26. K. Kim, S. Lee, J. Yoon, J. Heo, C. Choi, and Y. Park, Sci. Rep. **6**, 36815 (2016).
27. T. C. Wedberg and W. C. Wedberg, J. Microsc. **177**, 53 (1995).
28. B. Simon, M. Debailleul, A. Beghin, Y. Tourneur, and O. Haeberlé, J. Biophoton. **3**, 462 (2010).
29. K. Kim, H. Yoon, M. Diez-Silva, M. Dao, R. R. Dasari, and Y. Park, J. Biomed. Opt. **19**, 011005 (2014).
30. C. Liu and Y. Yin, Opt. Express **24**, A104 (2016).
31. J. Jung, K. Kim, J. Yoon, and Y. Park, Opt. Express **24**, 2006 (2016).
32. M. K. Kreysing, T. Kießling, A. Fritsch, and C. Dietrich, Opt. Express **16**, 16984 (2008).
33. M. Habaza, B. Gilboa, Y. Roichman, and N. Shaked, Opt. Lett. **40**, 1881 (2015).
34. B. Le Saux, B. Ghalmond, Y. Yu, A. Trouvé, O. Renaud, and S. L. Shorte, J. Microsc. **233**, 404 (2009).
35. M. Habaza, M. Kirschbaum, C. Guernth-Marschner, G. Dardikman, I. Barnea, R. Korenstein, C. Duschl, and N. T. Shaked, Adv. Sci. **4**, 1600205 (2017).
36. T. Zhang, C. Godavarthi, P. Chaumet, G. Maire, H. Giovannini, A. Talneau, M. Allain, K. Belkebir, and A. Sentenac, Optica **3**, 609 (2016).